energies

MDPI

Article

Quantitative Characterization of Pore Structure Parameters in Coal Based on Image Processing and SEM Technology

Mingyue Jia [1], Wenhui Huang [1,2,*] and Yuan Li [1]

[1] Key Laboratory for Marine Reservoir Evolution and Hydrocarbon Abundance Mechanism, School of Energy Resources, China University of Geosciences (Beijing), Xueyuan Road No. 29, Haidian District, Beijing 100083, China
[2] Coal Reservoir Laboratory of National Engineering Research Center of CBM Development & Utilization, China University of Geosciences (Beijing), Xueyuan Road No. 29, Haidian District, Beijing 100083, China
* Correspondence: huangwh@cugb.edu.cn

Abstract: The pore structure parameters of coal have an important influence on the exploration and development of coalbed methane. In this study, a series of pore structure parameters, including porosity, pore radius, pore throat radius, pore coordination number, pore throat ratio, and specific surface area, are identified, extracted, and calculated in the scanning electron microscopy (SEM) images of coal reservoir samples using algorithms and application programs in MATLAB. Constant rate-controlled mercury injection and low-temperature N_2 adsorption experiments were carried out to determine the accuracy of the SEM image-based processing analysis results. Characterization results show that the distribution of pore radius in the target coal samples of different organic matters range from 15 nm to 500 μm with porosity of 1.87–8.31% and radius distribution of 12.7 nm to ~100 μm. A noise-reduction system was constructed to eliminate the optical noise of non-porous features and repair the space affected by binarization noise. It is suggested that the characterization processing in this study is suitable for coal or other organic-rich porous materials with porosity > 2% and pore radius > 15 nm.

Keywords: computed tomography; porous throat; image analysis; coal; pore structure

Citation: Jia, M.; Huang, W.; Li, Y. Quantitative Characterization of Pore Structure Parameters in Coal Based on Image Processing and SEM Technology. *Energies* **2023**, *16*, 1663. https://doi.org/10.3390/en16041663

Academic Editor: Hossein Hamidi

Received: 6 January 2023
Revised: 29 January 2023
Accepted: 1 February 2023
Published: 7 February 2023

1. Introduction

The pore space of coal is the storage place and migration channel of groundwater and coalbed methane. The number of the pores, the size of a single pore, the characteristics of pore distribution, and the connectivity of pore space in coal reservoirs and coal seam-related reservoirs directly affect the migration and accumulation of coalbed methane [1,2]. It is of great significance to explore the pore characteristics and distribution of coal reservoirs for the exploration and development of coalbed methane. The pore characteristics of coal reservoirs include pore type, structure, size, quantity, and connectivity [3–6]. The study of coal pore structure mainly covers various aspects such as pore radius distribution, pore throat characteristics, pore type, porosity, poor connectivity, and specific surface area.

At present, two conventional methods are used to characterize the pore structure of coal or other porous media: direct observation methods and indirect measurement methods. Direct observation methods include BIB-SEM, FIB-SEM, and atomic force, while indirect measurement methods are mercury injection, gas adsorption, small-angle scattering, and NMR T2 spectrum [7–10]. Direct observation methods such as SEM and micro-CT use instruments to observe pores in the coal reservoir directly in 2D and 3D and obtain quantitative pore structure information and parameters by statistical methods or computer software [11–13]. Transmission electron microscopy and scanning electron microscopy can directly observe the pores of coal reservoirs, but cannot quantitatively identify pore structure parameters [14,15]. Three-dimensional X-ray CT imaging technology is a novel

approach for determining the structural parameters of coal reservoirs [16,17]. It is a non-destructive testing technology that identifies the internal structure of materials and obtains the reconstruction of CT scanning images of samples by using the attenuation of intensity after X-rays pass through materials [1,18]. Coal geologists use modelling technology and image reconstruction technology to quantitatively study these CT images with pore structure parameters [19–21]. The detailed characteristics of different methods are listed as follows (Table 1).

Table 1. Quantitative analysis methods for pore throat parameters of coal.

Analysis Methods		Parameters	Characteristics
Direct observation methods	SEM (Scanning electron microscope)	Nanoscale pore-throat radius (<1 μm)	Convenient but partial; Quantitative parameters need to be combined with computer software or other methods
Indirect experimental methods	Mercury injection	Porosity, pore-throat radius (<2 μm)	Convenient but inaccurate
	Nuclear magnetic resonance	Porosity, content of mud cement	Content of the whole sample; relatively precise
	Radiation X-ray computed tomography	3D pore-throat distribution and coordination number	3D pore-throat distribution is perfectly measured; expensive
	N_2 gas adsorption	Specific surface area, pore-throat radius	Connected pore is well measured
	X-ray diffraction	Content of calcite and mud cements	Content of the whole sample; relatively precise

Although indirect measurements, with high-pressure mercury injection and gas adsorption experiments as conventional methods, cannot obtain the morphological distribution of coal reservoir pore structure, they can carry out various pore parameters including pore radius, pore throat distribution, porosity, and specific surface area [22,23]. In mercury injection experiments, pore size distribution of the reservoir is obtained by measuring the mercury injection pressure and volume. When mercury enters pores connected to the pore throat with only a small throat, the volume of the small pore will be overestimated. At the same time, when the mercury injection method is used to measure the nanoscale pore, it may damage the nano-sized pore due to the excessive pressure required. The mercury injection experiment can only accurately measure the pore throat above 15 nm. The gas adsorption analysis has a long test time, with a testing range of pore between 0.3 and 200 nm. Moreover, for the same sample, the pore size distribution characteristics obtained by using different calculation models are quite different [24]. Yao et al. [2] proposed a method for quantitative analysis of different pore structures and types in coal using the morphology of the NMR T2 spectrum, but it can only test the pore structure characteristics of connected pores in coal and is hard to quantitatively analyze the closed pores in coal [25,26]. The limitations, uncertainties, and applicability of various methods have brought great difficulties to the quantitative analysis of nanoscale and microscale pores in coal reservoirs.

Image-based analysis methods are widely applied to determine various structure parameters of sand, shale, soil particles, and nanomaterials in 2D and 3D by software, algorithm, and function-based models and numerical simulation [27–29]. Combined with X-ray computed tomography (CT), the automatic image recognition for SEM, core sample, thin section images, and CT images play a significant role in the analysis of the microstructure of various materials [30–33]. This paper identifies, obtains, and calculates the porosity, pore radius, pore throat radius, pore coordination number, pore throat ratio, and specific surface area of coal samples based on SEM images and functions, algorithms, and application programs in MATLAB. Coal samples from the Qinshui Basin of China were selected for this study.

2. Sample and Methodology

2.1. Sample

Twelve samples of the No. 3 coal seam and No. 15 coal seam in the south of Qinshui Basin were selected for petrological observation and pore structure parameter determination. There are 10 to 16 coal seams in Qinshui Basin, among which No. 1–No. 5 belong to Shanxi Formation and No. 6–No. 16 belong to Taiyuan Formation. The main minable coal seams are No. 15, No. 9, and No. 3, of which No. 15 and No. 3 are stable and minable in the whole area, and No. 9 is partially minable. The No. 3 coal samples are black in bulk shape, with semi-bright coal as the main coal and mixed with a few semi-dark coals. The No. 15 coal seam is black, with bright coal as the main component, and dark coal is the secondary component. To better understand the whole quantitative analysis of various pore structure parameters based on the SEM image of the coal reservoir, we established the flow chart as shown in Figure 1.

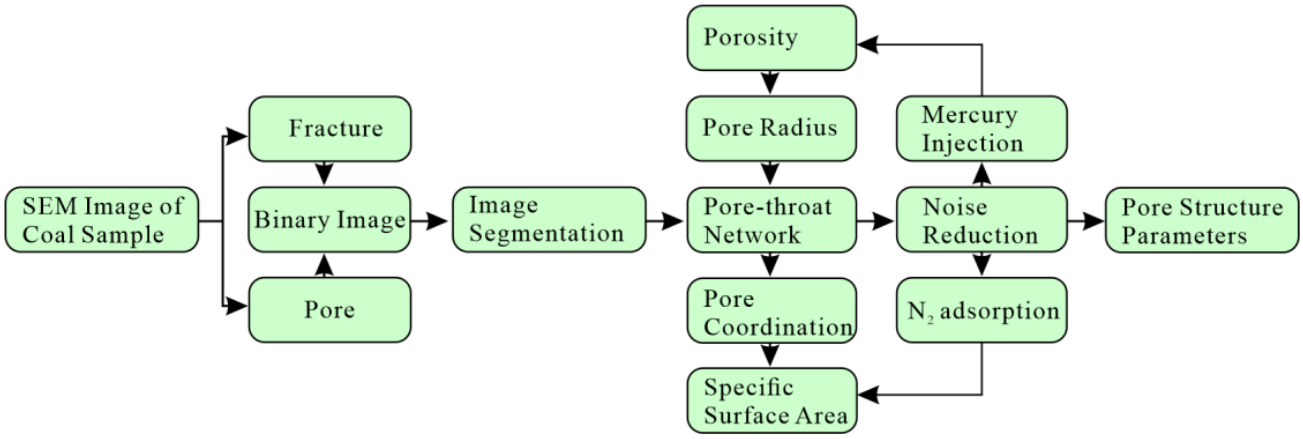

Figure 1. The flow chart of quantitative analysis of various pore structure parameters based on the SEM image of the coal reservoir.

2.2. SEM Image

SEM images with high resolution are often used for pore structure reconstruction and pore structure analysis [18,19]. The scanning electron microscopy was carried out with an S-4800 cold field emission scanning electron microscope produced by Japan HITACHI company and Czech TESCAN-VEGA/LSH thermal field emission scanning electron microscope to observe the pore characteristics and distribution after gold plating of coal samples. To explore the applicability of the algorithm–image quantitative analysis to various pores in coal samples, six types of pores in the coal sample were selected as the basic images: residual pores filled with quartz, pores in filamentous bodies, pores filled with kaolinite, matrix micropores, pores filled with kaolinite-illite, and plant cell pores filled with pyrite (Figure 2).

2.3. Image Binarization

To extract and obtain the pore information and distribution in the image, we first binarized the SEM images of the coal sample and transformed them into a binary image, which could be recognized by MATLAB. The methods for binarization mainly include feature-binarization analysis based on programming software and image binarization analysis. A single threshold setting can satisfy the processing of an image but using a threshold or a parameter to control a series of binary images will inevitably cause the results to deviate. The SEM image is a grey image that is not black or white. To improve the accuracy of image feature binarization, the original SEM is transformed into an adaptive image with an RGB color gamut. The adaptive threshold is set such that when different parts of the same image have different brightness, the threshold at this time is calculated based on each small area or unit on the image corresponding to the threshold. Taking

SEM images of matrix micropores as an example (Figure 3A), the division of sub-regions is carried out in MATLAB's built-in application, "Image Segmenter" (Figure 3B). The function "multithresh( )" is a function of segmenting image pixels, which is used to evaluate the gradient of a multi-scale greyscale image. The specific algorithm is as follows:

level = multithresh(P,L);

C = imquantize(B,level);

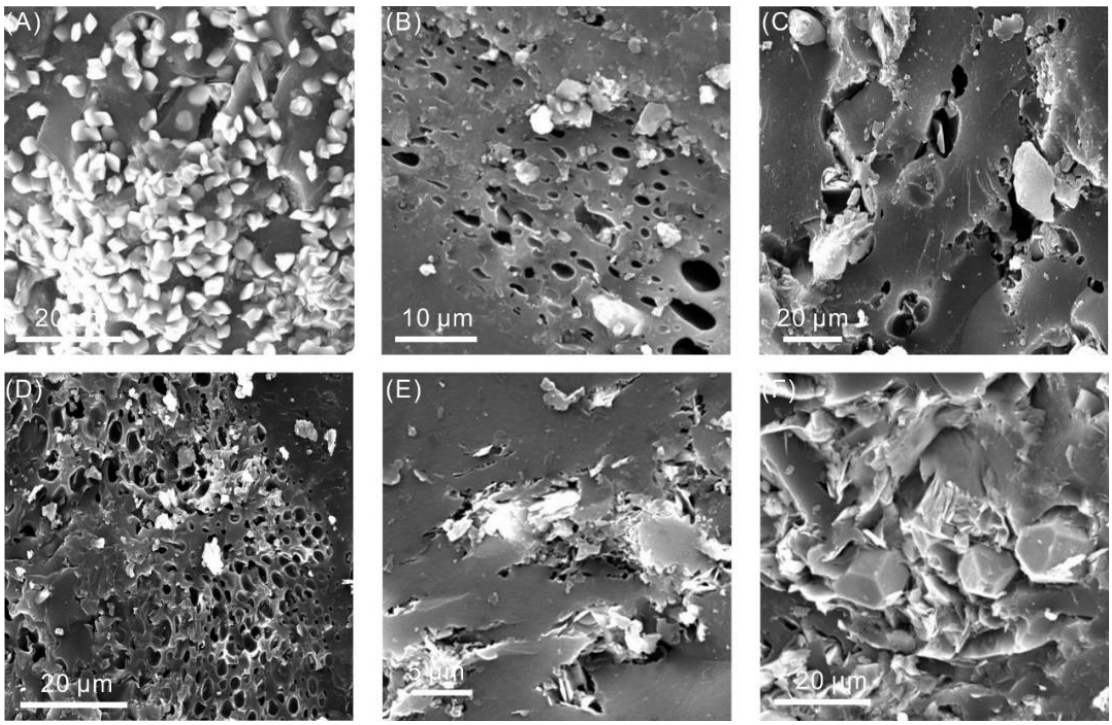

Figure 2. SEM images showing types of pores in a coal sample. (**A**) SX006-15, 1095 m, residual pores filled with quartz; (**B**) SX017-3, 993 m, pores in filamentous bodies; (**C**) BF3-1, 765 m, pores filled with kaolinite; (**D**) WZ3-3, 232 m, matrix micropores; (**E**) SGJ-15, 286 m, pores filled with kaolinite-illite; (**F**) WTP-15, 644 m, plant cell pores filled with pyrite.

P is the matrix value transformed by the input image. L is the number of grey levels divided. The function "imquantize" inversely assigns the obtained multi-scale greyscale image to the predecessor image of the adaptive binary image that we want. By adjusting the parameters in the "Image Segmenter", the SEM image is segmented by suitable units and then transformed into an adaptive threshold image by imquantize (Figure 3C). The final binary image is shown in Figure 3D. In the whole process, the binary image only retains the pore space in the image, which is also the basis for ensuring the accuracy of the entire process. Different thresholds are used in different areas of the same image so that we can obtain better results under different brightness conditions.

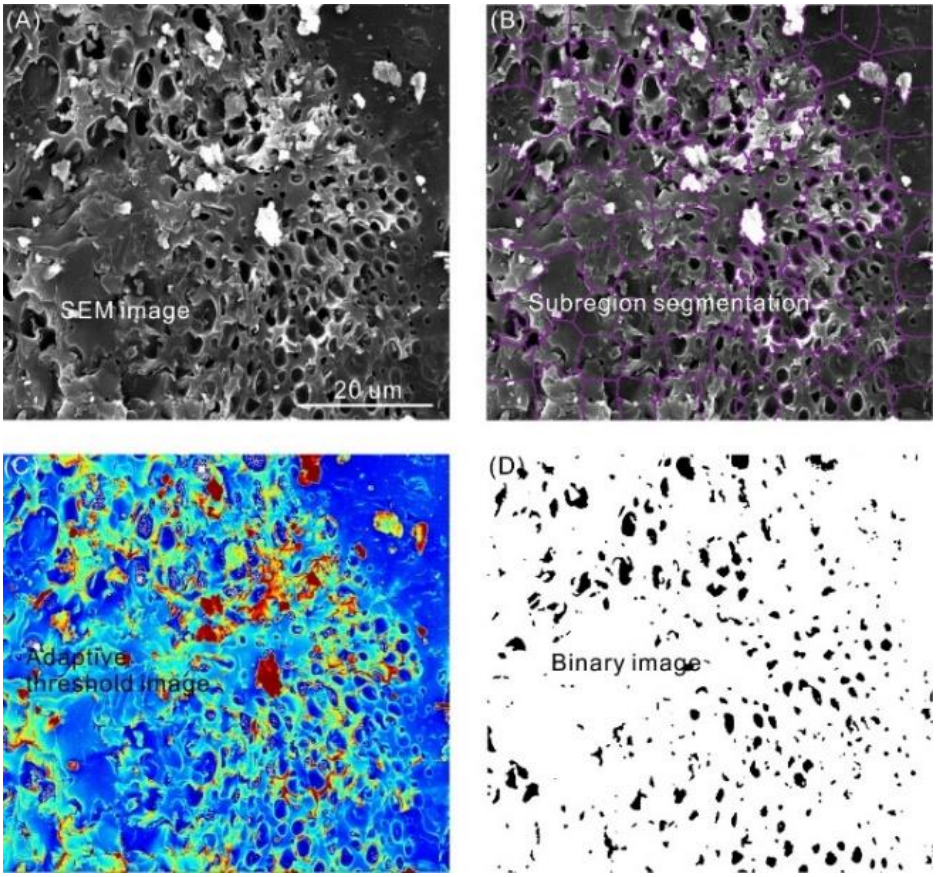

Figure 3. The binarization process of a SEM image: (**A**) WZ3-3, 232 m, matrix micropores; (**B**) Sub-region segmentation of (**A**); (**C**) Adaptive threshold image of (**A**); (**D**) Binary image of (**A**).

2.4. Segmentation of Pore Space

Segmentation is a basic but quite important step for image analysis. The segmentation result is fundamental to all subsequent processes and determines all subsequent calculations [34–36]. After image binarization, the most urgent task is to recognize the pore information in the binary image and convert it into the parameters that could be calculated. The function "bwperim" can be used to detect the position of sudden change or mutation points of the pixels in the binary image, which is the boundary between the pore and the macerals. The boundary of pore space is identified by the function "P = bwperim(C)". This step is to prepare for the calculation of porosity and pore surface area. For the acquisition of pore structure radius, pore throat distribution and pore coordination number, every pore unit in the binary image needs to be divided and restored to what they are in SEM images. The "bwlabel" function is used to segment the mutation points in a binary image, and the "regionprops" function is used to measure the attributes of the image region in MATLAB. Further, the functions of "label", "regionprops" and "bwlabel" are used to identify and divide the pore units.

$$[L,num] = bwlabel(C, N)$$

$$P = regionprops(C, bwlabel)$$

where C is the input image, N can be 4 or 8 to connect four connected or eight connected regions. "num" is the number of connected regions found; L is the output image matrix. The background elements in the binary image are marked as 0; the first connected region is marked as 1; the second connected region is marked as 2, and so on. All the steps in Section 2.4 are prepared for the following calculation of pore structure parameters.

2.5. Quantitative Analysis Process

2.5.1. Porosity of Coal Reservoir

The porosity of a coal reservoir is defined as the proportion of pore space in a unit area. The acquisition of pore area in the binary image is the key to calculating component content and porosity. There are two ways to obtain the image area in MATLAB using function "sum" or function "area". Function "sum" can sum the elements of each column and row of the matrix, while function "area" can sum the whole matrix of the binary image based on other algorithms. In this paper, function "sum" is selected for calculation, and the algorithm is as follows:

$$A_w = \text{sum(sum(White))}; \%\text{Pore area;}$$

$$A_{w+b} = \text{sum(sum(White) + sum(Black))}; \%\text{Total area;}$$

Then porosity "Φ" is:

$$\Phi = A_w/(A_w + A_b); \quad (1)$$

White or pore space is the white part of a binary image. Black or non-pore space is the black part of a binary image.

2.5.2. Pore Radius

To obtain the distribution of pore radius in SEM images, we need to calculate the radius of each pore unit that was divided in Section 2.4. The pore radius corresponds to half of the average of the major and minor axes of a single pore unit. The key of this step is to calculate the length of the major axis and minor axis of each element in the image, that is, the pore radius = (major axis radius + minor axis radius)/2. We establish a coordinate system for the image and try to find the maximum X coordinate (Xmax), minimum X coordinate (Xmin), maximum Y coordinate (Ymax), and minimum Y coordinate (Ymin) of each unit. The algorithm "ginput()" is a function that can obtain the coordinate value of a specified point in the X direction or Y direction. Based on the ginput(), Xmax, Ymax, Xmin, and Ymin of each unit pore can be obtained. The major axis length of each pore unit is (Max ['Xmax-Xmin', 'Ymax-Ymin']) and the minor axis is Min ['Xmax-Xmin', 'Ymax-Ymin']. The pore unit radius "R_p" is as follows:

$$\begin{aligned} Rp = [(Xmax\text{-}Xmin) + (Ymax\text{-}Ymin)]/2 = [&(ginput(Pn,maxx) - ginput(Pn,minx)) + \\ &(ginput(Pn,maxy) - ginput(Pn,miny))]/2 \end{aligned} \quad (2)$$

Pn is each pore unit identified in the binary image.

2.5.3. Pore-Throat Radius

Unlike the pore radius, the throat radius refers to the radius at the junction of two pore units. The junction of two pore units is the position of a line made up of pixel mutation points. The function "bwdist" is used to calculate the distance between elements. Function "regionprops" is defined to obtain the properties of the region, which is a function used to measure the properties of units of image. Many properties could be calculated by "regionprops", such as "area", "perimeter", "volume", "length", "centroid", etc. These two functions were combined to calculate the throat radius in conjunction as well as the pore-throat. Based on the segmentation results in Section 2.4, the following algorithm is adopted for each pore unit.

$$\begin{aligned} B &= \text{double(watershed(bwdist(A),255))} \\ Rt &= \text{regionprops(bwlabel(B), length);} \end{aligned} \quad (3)$$

A is the shortest distance between the position of zero pixels and the position of the non-zero pixel; 255 is the point where the nearest pixel near the element is 255.

After the pore radius and throat radius are obtained at the same time, the pore throat ratio in the coal sample can also be calculated.

$$\text{Pore throat radio} = Rp/Rt; \tag{4}$$

2.5.4. Acquisition of Pore Throat Network and Coordination Number

The pore throat coordination number of a coal reservoir refers to the number of throats connected to each pore in the coal sample. The coordination number reflects the degree of connectivity between pore space and pore throat. The higher the coordination number, the better the reservoir. In the segmentation unit of the binary image, the coordination number of the pore throat is equivalent to the number of pore units in which a single pore unit connects with the surrounding pore units. "Network" is the function connecting the panel points of pixel change in the image. Based on the pore unit of binary images, the algorithm "network = zeros ()" is used to calculate the pore throat coordination number. The network function is the function connecting the pixel nodes in the image.

```
Network = zeros(max(B(:)));
for I = 1:size(E,1)
Network(E(I,1),E(I,2)) = 1;
Network(E(I,2),E(I,1)) = 1;
```
(5)

2.5.5. Specific Surface Area

The formula for calculating specific surface area is defined as unit area/unit volume (m^2/m^3), while for 2D images, the specific surface area of pores is the ratio of perimeter and area in one unit, that is, m/m^2. Based on the binary image, we calculate the specific area of the identified pores. The perimeter of pore space in the binary image can be obtained by use of the function "regionprops" which measures the attributes of the image region in MATLAB as mentioned before. The pore area is obtained by A_w = sum(sum(White)). Then, the specific surface area is as follows:

```
Sp = regionprops(image, perimeter)
Specific surface pores in 2D = Sp/Resolution/Aw;
```
(6)

2.6. Mercury Injection Experiment

A constant velocity mercury injection experiment was performed with Autopore IV9500 Mercury Porosimeter to test the pore throat radius of coal samples. The maximum test pressure of 35 MPa and the radius of the roar channel can be tested in the range of 18–183,132 nm. The range of pore-radius can be tested between 18 nm and 183,132 nm with the highest test pressure of 35 MPa. The parameters of the pore structure tested by the mercury injection experiment include discharge pressure, average pore throat diameter, mercury injection saturation, and mercury removal efficiency. The pore-throat radius is determined by the pressure at the breakthrough point, and the pore radius is determined by mercury injection saturation.

2.7. Low-Temperature N_2 Adsorption

Due to the shortcomings of nano-sized adsorption pores and specific surface area of mercury injection experiments, research on pore parameters of coal reservoirs needs to be carried out in conjunction with the low-temperature N_2 adsorption test. The low-temperature N_2 adsorption test was performed with a Tristar23020 Low-temperature liquid N_2 adsorption instrument and Quadrasorb SI specific surface analyzer. The N_2 adsorption experiment was operated at a saturation pressure of 77.35 K, using liquid nitrogen with a purity of more than 99.999% as the adsorption medium, and at a relative pressure of 0.01 to 0.995. The whole experiment is suitable for measuring pores with a pore diameter of less than 10 nm. The smallest pore radius measured can only reach about 0.6 nm, and the

largest measured pore diameter ranges from 100 nm to 150 nm. Both the constant rate mercury injection experiment and the low-temperature N_2 adsorption test were carried out at North China Petroleum Exploration and Development Research Institute.

3. Results and Discussion

3.1. Parameters of Pore Structure

3.1.1. Porosity of Coal Reservoir

Based on the binarization process in Section 2.3, images obtained in Figure 2 were transformed into the adaptive threshold images (Figure 4). In Figure 4, red represents pore space, while blue is the matrix and macerals. Furthermore, the application program "Image Segmenter" is used to binarize the self-adaptive images of various pore types. The binary images with pore space characteristics can be obtained. As discussed before, the key step in the process of obtaining the porosity of coal samples based on SEM images is to obtain the pixel area of pore space by function "sum". Through Formula (1), the porosity in SEM images of all kinds of coal samples is obtained. The porosity of binary images in Figure 4 is 1.2662%, 5.2181%, 6.2559%, 8.3128%, 4.5052% and 7.9579% for panels A–F, respectively.

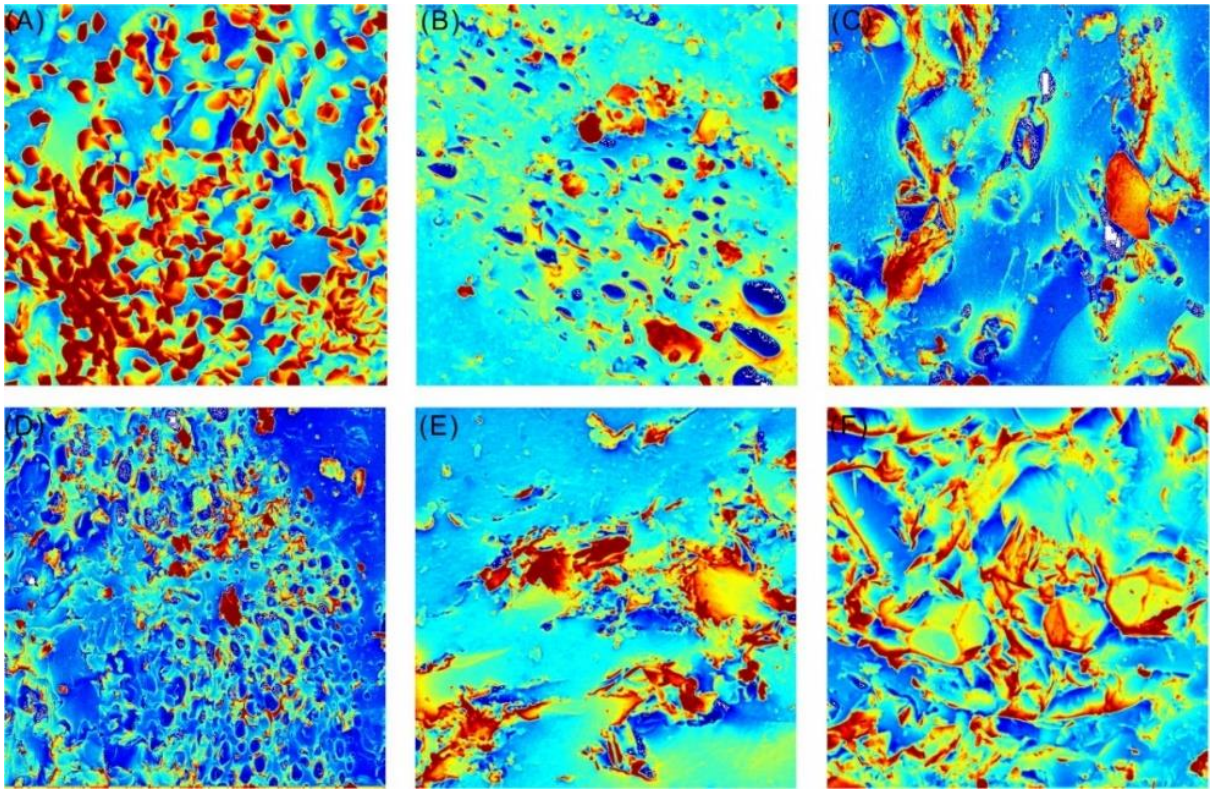

Figure 4. (**A**–**F**) Adaptive threshold images corresponding to Figure 2A–F.

3.1.2. Pore Radius of Coal Reservoir

The distance between any pore center point on the central axis of the coal reservoir and the rock skeleton is defined as the pore radius. The pore radius reflects the reservoir's storage capacity [37,38]. Based on the pore unit segmented by binary image, the pore radius of the coal reservoir can be obtained by Formula (2). Because the pore space in coal is mainly composed of nanoscale pores, the pore space is divided between the *X*-axis and *Y*-axis by applying the related algorithms of functions "bwperim" and "regionprops" (Figure 5A–F). Further, the long-axis radius and the short-axis radius of various types of pore units are calculated using Formula (2). The average radius of the various pores is: 3.1117 μm, 3.8228 μm, 2.1059 μm, 1.2771 μm, 5.7849 μm, 7.5580 μm and the corresponding distribution of pore radius is displayed in Figure 5G–L.

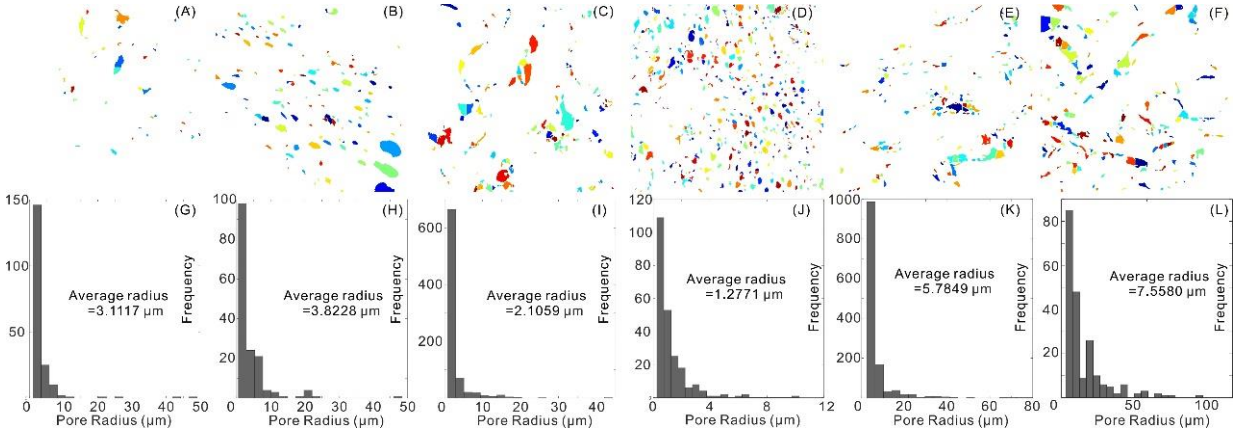

Figure 5. Pore unit segmentation (**A**–**F**) and pore radius distribution (**G**–**L**) corresponding to Figure 2A–F.

In addition to the pore space, various fractures also play an important role in the permeability and storage of coal reservoirs. Fractures are endogenetic or exogenetic. Endogenetic fractures, also known as cleavage, are formed by uniform shrinkage of the volume of coal-forming materials, which causes tension along the coal seam (Figure 6A). Exogenic fractures are formed by geological stress, including tensile exogenic fracture and shear exogenic fracture (Figure 6B,C). The algorithm-image quantitative analysis designed in this paper is also suitable to calculate the radius of various fractures. Based on the SEM image and thin section image, the radius of the endogenetic crack, micro-crack, tensile exogenetic crack, and shear exogenetic crack are extracted and calculated. Based on the analysis of Section 2.5.2, the whole analysis process is similar to the calculation of the pore radius of coal reservoir in principle. The adaptive threshold segmentation and binarization of the image are carried out successively, and the binary image obtained is calculated. Calculation results of four types of crack radius in Figure 6I–L are 2.2368 μm, 6.8697 μm, 10.5677 μm, and 6.0612 μm, respectively.

3.1.3. Pore-Throat Radius

The pore throat radius is the length of the contact point between two connected pores in the reservoir. The radius of the pore throat in different types of reservoir space is a crucial factor in determining reservoir permeability. The principle of calculating the pore radius and pore throat radius of coal reservoirs based on SEM images is also completely different. According to the discussions in Sections 2.5.2 and 2.5.3, the key point of calculating the pore throat diameter is how to capture the position of the pore throat. The combination of functions "bwdist" and "regionprops" and Formula (3) solves this problem perfectly. Using the function "regionprops" to identify the color change of different pore units in Figure 7, and relying on the function "bwdist" and Formula (3) to calculate the identified mutation lengths consisting of mutation points, the length of the pore throat radius can be calculated.

To visually discern the calculated length of the pore throat radius, Figure 8A–F shows the identification points of various pore throat diameters. The pore-throat radius in Figure 8G–L are calculated by Formula (3) and the average pore throat radius corresponds to 1.8831 μm, 1.32411 μm, 1.2693 μm, 0.9789 μm, 0.5662 μm, and 1.1760 μm. After obtaining the average pore radius and an average pore throat diameter of the coal radius, Formula (4) can be used to calculate the pore throat ratio of the coal reservoir, namely, the pore throat ratio = average pore radius/average pore-throat radius.

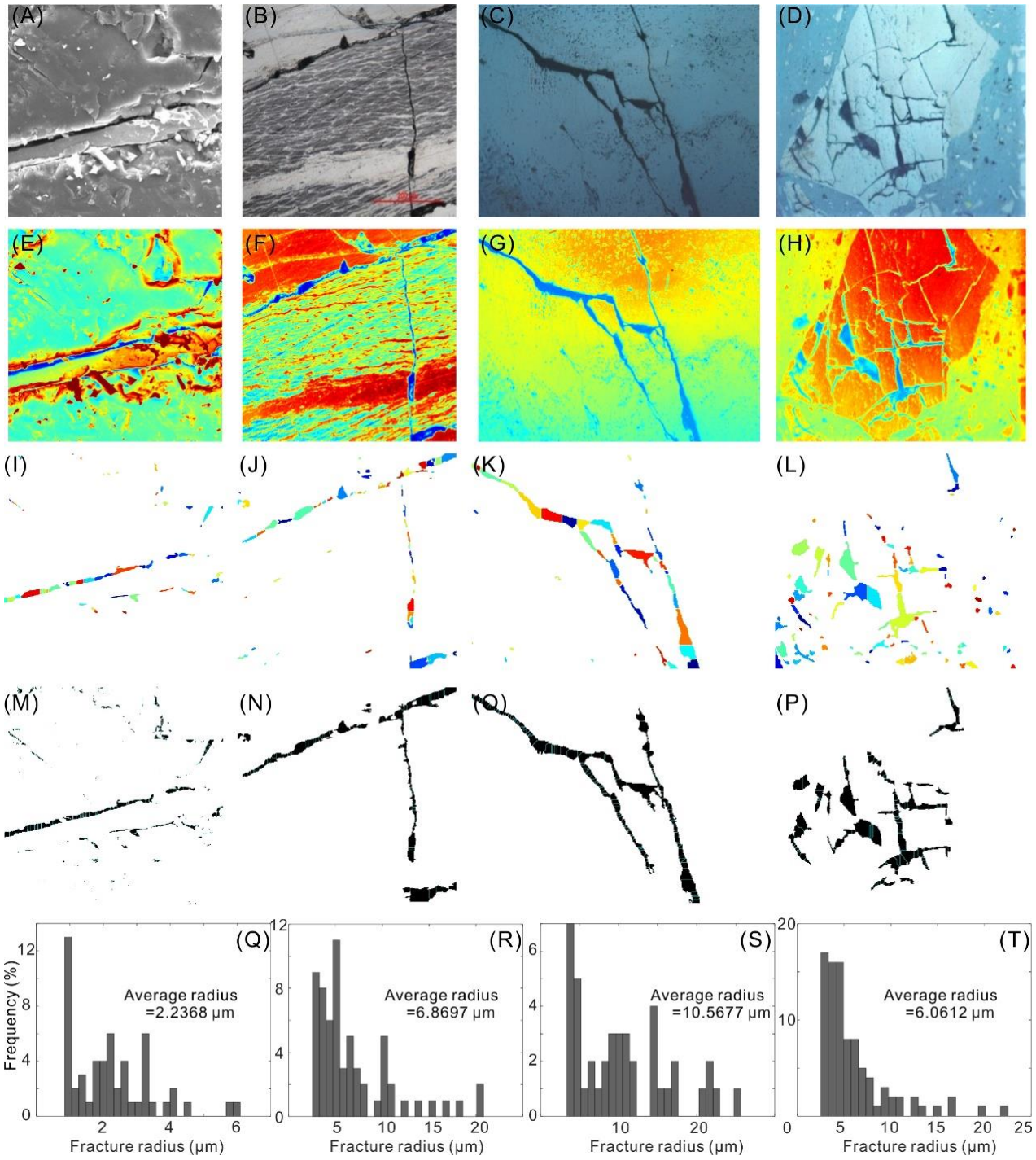

Figure 6. SEM images showing fracture types: (**A**) SX015-5, fracture filled by calcite; (**B**) WZ03, micro-fractures; (**C**) SX306-23, tensional fracture; (**D**) SX008-2, shear fracture. (**E**–**H**) Adaptive threshold images of (**A**–**D**); (**I**–**L**) pore unit segmentation images of (**A**–**D**); (**M**–**P**) pore radius identification of (**I**–**L**); (**Q**–**T**) pore radius distribution of (**A**–**D**).

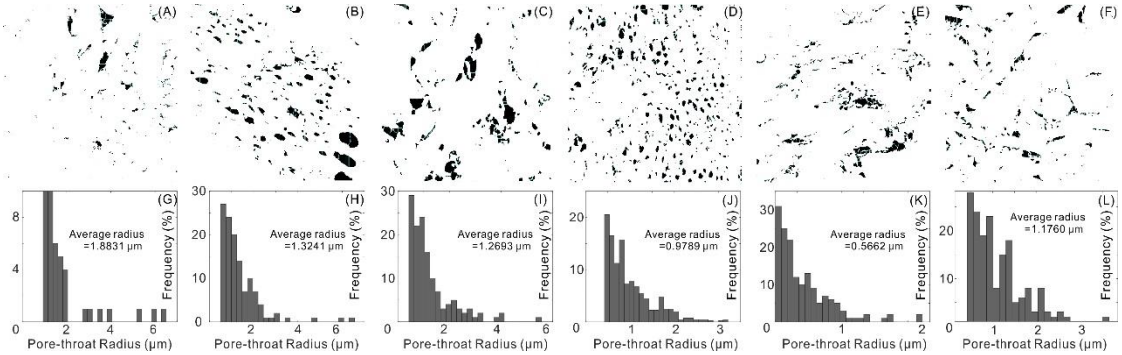

Figure 7. Visual output of the pore-throat of SEM image in Figure 1 with the blue line (**A**–**L**) correspond to Pore radius distribution of (**A**–**F**).

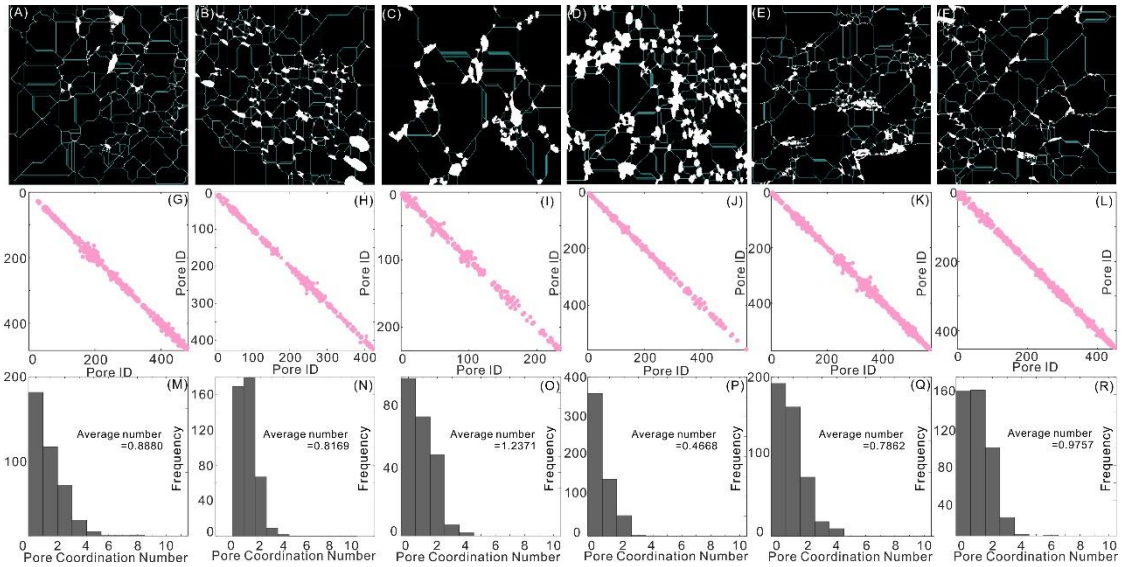

Figure 8. Coordination distribution of different types of pores in Figure 2 (**A**–**F**); Coordination results of pore units between pore IDs of Figure 6 (**G**–**L**); Pore-throat coordination number distribution of Figure 9G–L (**M**–**R**).

3.1.4. Coordination Number

The topological structure of pore space in a coal reservoir refers to the connection relationship or connectivity between each pore throat in the rock. The number of the single pore-throat unit connected with other pore-throat units in the coal sample is called pore throat coordination number, which is generally between 1 and 5. The distribution of pore throat coordination numbers reflects the connectivity of the pore network model. The connectivity between pores and throats has a great influence on the displacement process of coalbed methane. The higher the coordination number, the better the connectivity, the more fluid migration channels, and the better the reservoir properties. The average pore throat coordination number is used to reflect the connectivity of coal reservoirs. On the basis of the distribution of the pore segmentation unit, the pore network and nodes in Figure 6 are identified by the function "network" and the related algorithm in Section 2.5.4. The results of identification are shown in Figure 8G–L. Each pore ID in the image represents each pore segmentation unit, so the recognition of pore throat coordination is transformed into the match of the pore ID. Formula (5) is applied to calculate the coordinate number with the output image of the segmented pore cell (Figure 8).

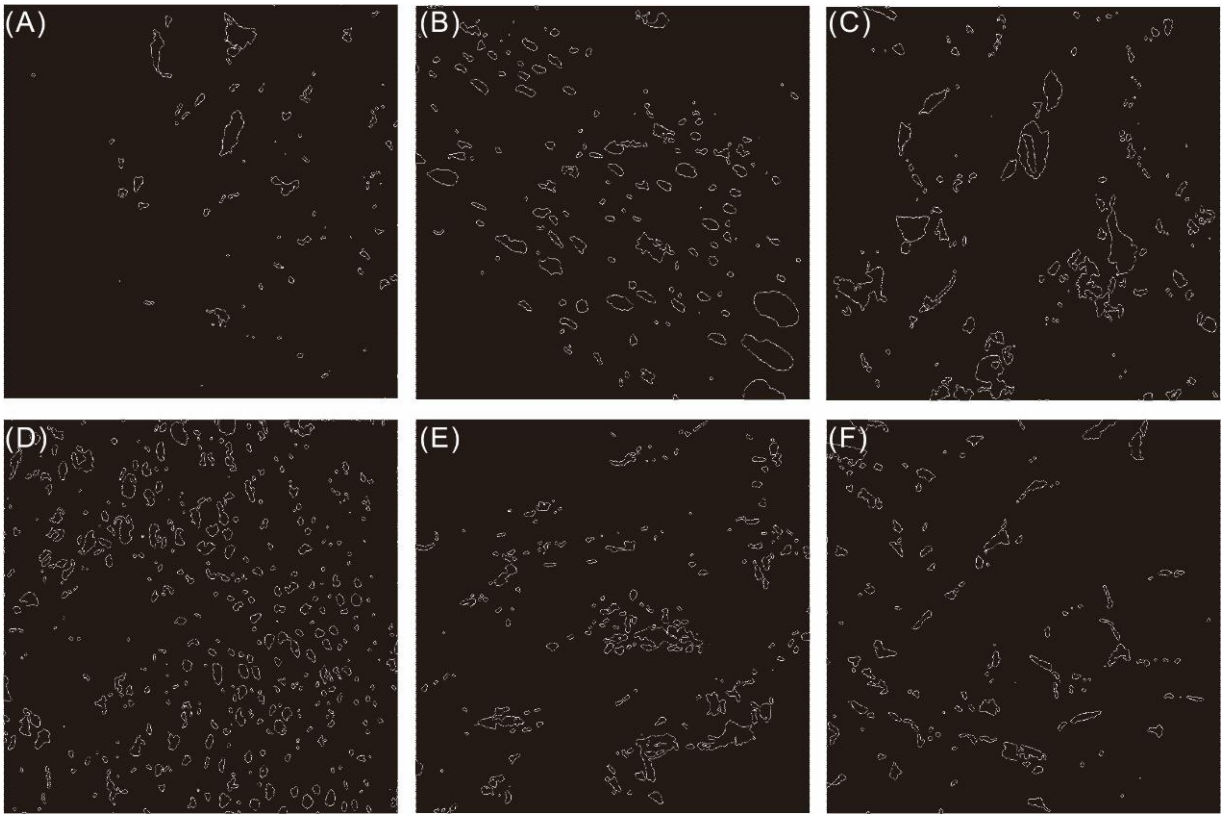

Figure 9. The average specific surface area of threshold image in Figure 2A–F corresponding to (**A**–**F**).

3.1.5. Specific Surface Area

Specific surface area is defined as the total area of a unit mass of material with the unit of m^2/g. There are two types: external specific surface area and internal specific surface area. Specific surface area is one of the important reference indexes for evaluating the industrial utilization of catalysts, adsorbents, and other porous materials such as asbestos, mineral wool, and clay minerals. Coalbed methane is mainly adsorbed on the inner surface of the coal matrix, and micropores are the main part of gas adsorption. The specific surface area has an important effect on the adsorption capacity of reservoir rocks. According to the physical adsorption theory of solid surfaces, the adsorption capacity is directly proportional to the specific surface area. The size of a coal reservoir' specific surface area has a significant impact on the thermal properties, adsorption capacity, chemical stability, heterogeneity of the reservoir, and CBM's development and utilization. Currently, for the measurement of the specific surface area of the pores we use the functions "sum" and "regionprops" to obtain the surface area and perimeter of the pore space in the binary image and calculate the specific surface area of the pore space on the plane or in the two-dimensional space by Formula (6). The average specific surface area of pores in Figure 9 corresponding to the original images of Figure 5 is 1.8705 m^2/g, 0.9747 m^2/g, 0.9502 m^2/g, 1.1635 m^2/g, 1.2852 m^2/g, and 1.3065 m^2/g. Table 2 shows the data calculated based on quantitative analysis.

3.2. Mercury Injection Data

The results of the mercury injection test (Table 3) show that the average pore content of coal samples in Qinshui Basin is 84.70% with a pore radius smaller than 100 nm (micropores), 9.52% with pore radius of 100 to ~1000 nm (middle pores), and 4.23% with pore diameter larger than 1000 nm (large pores). In the No. 3 coal seam, the proportions of micropores, middle pores, and large pores are 85.38%, 9.08%, and 3.96%, respectively. In the No. 15 coal seam, the proportions of micropores, middle pores, and large pores are 83.36%, 10.39%, and 4.78%. The average mercury saturation of No. 3 coal samples

is 36.30%, and that of No. 15 coal samples is 44.98%, which indicates that the effective pore of the coal reservoir is less. The displacement pressure reflects the capillary pressure when mercury enters the maximum throat of the coal sample. The smaller the value is, the larger the pore-throat radius is. The average displacement pressure of coal seam No. 3 is 3.36 MPa, and that of coal seam No. 15 is 2.77 MPa. The mercury removal efficiency of coal samples in the south of Qinshui Basin ranges between 47.41% and 72.06%, mostly higher than 50%. The high mercury removal efficiency indicates that the pore connectivity is good. The average mercury removal efficiency of the No. 3 coal samples and No. 15 coal samples are 67.11% and 65.47%, showing that the pore connectivity of the No. 3 coal seam is better than that of the No. 15 coal seam. The pore structure parameters of the coal reservoir in the south of Qinshui Basin were measured by the constant velocity mercury injection method.

Table 2. Pore structure parameters calculated by image–algorithm quantitative analysis.

	Sample	Type	Porosity (%)	Pore Radius (μm)	Pore-Throat Radius (μm)	Coordination Number	Pore Throat Ratio	Pore Specific Surface Area (m^2/g)
1	SX006-15	Pore space	1.266	0.311	0.188	0.888	1.65	1.871
2	SX017-3		5.218	0.382	0.132	0.817	2.887	0.975
3	BF3-1		6.256	0.211	0.127	1.237	1.659	0.950
4	WZ3-3		8.313	0.128	0.098	0.467	1.304	1.164
5	SGJ15-1		4.505	0.579	0.056	0.786	10.22	1.285
6	WTP15-1		7.958	0.756	0.118	0.976	6.426	1.307
7	LDS-15	Fracture	2.059	2.237				
8	WZ3-2		3.199	6.870				
9	SX306-23		4.201	10.568				
10	SX008-2		7.059	6.061				

Table 3. Mercury injection data of coal reservoir samples in the south of Qinshui Basin.

Sample	Porosity (%)	Maximum Mercury Saturation (%)	Displacement Pressure (MPa)	Average Pore-Throat Radius (μm)	Mercury Porosimetry Percentage		
					0–100 nm	100–1000 nm	>1000 nm
WZ3-3	3.0	44.85	1.97	0.15	81.21	12.14	5.21
WY3-2	1.6	47.78	4.87	0.06	86.67	9	2.84
BF3-1	3.4	36.81	2.78	0.11	84.51	9.4	4.59
SX005-2	1.4	26.9	1.17	0.25	86.12	8.35	4.06
SX013-3	6.2	26.55	1.8	0.17	86.8	8.44	2.44
SX008-2	2.3	39.16	3.92	0.11	85.97	9.07	3.49
SX011-3	3.9	35.85	5.08	0.05	84.42	8.74	5.4
SX025-3	0.8	32.46	5.31	0.06	87.3	7.53	3.68
SGJ15-1	7.5	32.61	0.2	1.29	79.55	9.71	9.25
WTP15-1	1.6	60.28	2.34	0.11	81.04	14.03	3.48
FHS15-1	1.4	49.45	5.08	0.06	86.4	9.04	3.09
SX005-5	3.1	37.58	3.45	0.11	86.46	8.79	3.28
SX008-8	0.3	76.23	0.94	0.24	68.8	23.03	6.7

3.3. Low-Temperature N_2 Adsorption Data

The low-temperature N_2 adsorption can quantitatively analyze the nanocomposites in shale or coal reservoirs which are composed of porous mineral structures with a small radius [39,40]. Table 4 shows the data of low-temperature N2 adsorption. The BET-specific surface area of the No. 3 coal sample ranges from 0.345 m^2/g to 1.379 m^2/g, with an average value of 0.72 m^2/g. The average BJH cumulative specific surface area is distributed between 0.707 m^2/g and 2.723 m^2/g, with an average value of 1.764 m^2/g. The total BJH pore volume is 3.034×10^{-3} mL/g, with an average pore diameter of 15.05 nm. The average BET-specific surface area of the No. 15 coal sample ranges from 0.087 to 1.6832, with an average value of 0.543 m^2/g, and the average surface area of BJH is 1.543 m^2/g. The average BJH pore volume is 2.836×10^{-3} mL/g, with an average BJH pore diameter of 20.35 nm. The specific surface area and total pore volume of the two coal seams show a good distribution of pores, which can provide a larger adsorption area and volume. In addition, the specific surface area and total pore volume of No. 15 coal are slightly lower

than those of No. 3 coal, and the average pore diameter is slightly larger than that of the No. 3 coal sample. N_2 adsorption experiments rely on fluid pressure for pore simulation to obtain specific surface area parameters. During the process of fluid injection into the rock, the sudden increase in pressure may lead to the fracture of original rock pores or the formation of new pores affected by pressure, resulting in the change of specific surface area.

Table 4. Nitrogen adsorption data of coal reservoir samples in the south of Qinshui Basin.

Sample	BET Specific Surface Area (m^2/g)	BJH Cumulative Specific Surface Area (m^2/g)	BJH Total Pore Volume (mL/mg)	Average Pore-Throat Radius (nm)
WZ3-3	0.50	1.62	1.91	11.17
WY3-2	0.47	1.51	1.32	7.93
BF3-1	0.12	0.71	0. 90	23.18
SX005-2	1.25	2.21	4.47	12.88
SX013-1-3	1.38	2.72	6.35	16.08
SX008-2	1.31	2.55	5.83	16.04
SX011-3	0.35	1.54	2.24	21.06
SX025-3	0.40	1.26	1.36	10.58
SGJ15-1	0.31	1.63	1.71	16.77
WTP15-1	0.31	1.37	1.54	13.80
FHS15-1	0.32	1.11	1.37	13.04
SX0015-5	0.09	0.94	1.12	38.84
SX0015-8	1.68	2.66	8.53	19.29

3.4. The Generation and Reduction of Noise

3.4.1. Noise Reduction

A scanning electron microscope can observe nanoscale pores because of its super magnification. During the shooting process, the dark angle and optical noise caused by the high pressure, the SEM image will generate a certain amount of optical noise during the shooting process, which cannot be ignored for the impact of nanoscale and microscale pores. Due to the small radius of these optical noises, the specific surface area of each unit is very large, which greatly affects the distribution of pore and throat radius and the specific surface area. Therefore, it is necessary to perform noise reduction on the binary image obtained in Section 2.4. Noise reduction includes the elimination of noise without pore features and the compensation or repair of the space where the pores are removed due to the influence of noise. Function "imerode" and function "bridge" are used to eliminate and repair the noise effect. Function "imerode" is designed to remove isolated pixel areas, such as 255 pixel points surrounded by a zero pixel area. The function "bridge" is used to establish a bridge between disconnected pixels. For example, if there are two non-zero unconnected pixels, "bridge" will set the zero value pixel to 255. When applying these two functions, we must combine the function "bwmorph" which can identify the morphology of the image (the ability to perform digital morphology operations on binary images). The specific algorithm is as follows:

$$\begin{array}{c} P = \text{bwmorph(P,'imerode',n);} \\ P = \text{bwmorph(P,'bridge',n);} \end{array} \quad (7)$$

n represents the specified morphological processing on the binary image n times. n needs to be divided according to the actual pixels, generally set to one in this paper. It is worth noting that the order of function "imerode" and function "bridge" is fixed and cannot be reversed. If the noise is repaired first, more noise will be generated in the binary image, increasing the noise further.

3.4.2. Difference of Pore Structure Parameters before and after Noise Reduction

The strong heterogeneity of the pore structure of coal reservoirs in size, shape, distribution, and connectivity makes the noise reduction process more important for the

calculation of pore structure parameters. Taking the binary image of Figure 2D as an example, "imerode" and "bridge" are applied to reduce the noise. To distinguish the effect of noise reduction on pore parameters, we compare the performance of the pore structure in porosity, radius distribution, and connectivity before and after noise reduction. Figure 10A,B corresponds to the original binary image and the denoised image after image segmentation. It can be observed that the binary image after noise reduction is clearer in morphological performance, and the optical noise in the image is also eliminated. Affected by the accumulation and transitivity of the noise, the recognition results based on the pore unit segmentation image and the pore connectivity also show very large differences after noise reduction. Similarly, a large amount of optical noise in SEM will be mistaken for pore space by MATLAB, which will lead to the change of the pore distribution in Figure 10C,D. The most direct performance of the binary image after noise reduction is the decrease of porosity, which is reduced from 14.319% to 13.374%. The elimination of noise effects will also affect the parameters of pore radius and connectivity.

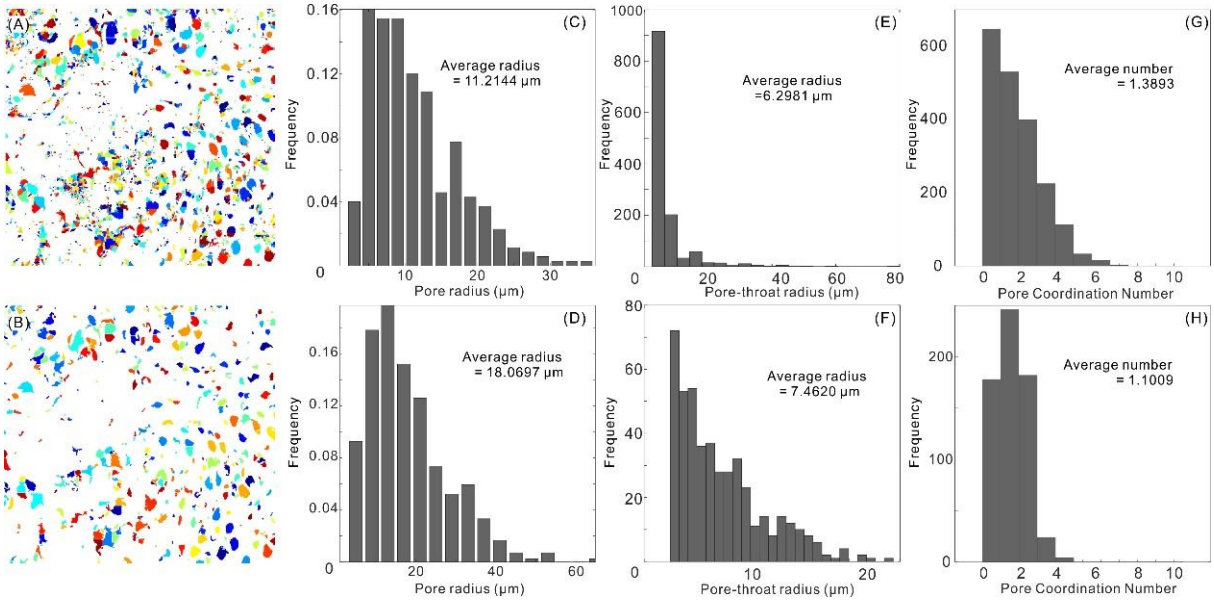

Figure 10. (**A**) The original pore unit segmentation; (**B**) Pore unit segmentation of the denoised binary image; (**C**,**D**) Pore radius distribution; (**E**,**F**) Pore-throat radius distribution; (**G**,**H**) Poor coordination number.

In the aspect of pore radius distribution, the pore radius in the noise-reduced binary image is significantly higher than that in the original binary image (Figure 10E,F). The average pore radius is 11.2144 μm and 18.0697 μm, respectively. Before noise reduction, the optical noise that exists inside the pore space makes a single pore space divided into multiple pore units. The pores with a large radius in SEM images are replaced by several pores with smaller radius pore units in the binary image. In terms of pore-throat radius distribution, similar to the pore radius, the pore-throat radius in the denoised binary image is slightly larger than that in the original binary image, respectively. The average pore throat radius of these two images is 6.2981 μm and 7.4620 μm. The reason for the increase of the pore-throat radius after noise reduction is the same as that of the pore radius. On the one hand, the initial pore space is divided into several pore individuals with smaller pore radius by optical noise, which is restored to individuals with a larger radius. On the other hand, noise with a smaller radius is also removed. Noise results in a large number of pore spaces being segmented, which also influences the calculation of pore coordination numbers. The average pore coordination numbers of the original binary image and the denoised binary image are 1.3893 and 1.1009, respectively. Therefore, when calculating the

pore structure parameters of coal reservoirs based on SEM images, the elimination of noise is an indispensable step and an important process.

3.5. Fitness

To explore the applicability of the image–algorithm quantitative analysis, we compared the porosity, pore throat radius, and BET specific surface area obtained in the mercury injection experiment and N_2 adsorption experiment. For the coal reservoir porosity, the porosity measured by image–algorithm quantitative analysis and the mercury injection experiment results shows a quadratic function distribution, with a symmetric axis of about 5% (Figure 11A). When the coal reservoir is less than 5%, there is a positive correlation between the two measurement results. When the coal reservoir is more than 5%, the image analysis results are larger than the mercury injection experiment results, showing a negative correlation. We speculate that two factors are affecting this distribution. First, the mercury injection experiment mainly obtains the connected pore space of the coal sample, while the image–algorithm analysis calculates the sum of all the pores in the SEM image, including the connected pores and the closed pores. However, this explanation is bound to lead to the data measured by image analysis being higher than the results of the mercury injection experiment. Second, the noise reduction of the binary image results in some unconnected pores or individual pores mistaken as noise by the algorithm, which makes the measured porosity lower than the real value. Therefore, when the porosity of the coal reservoir is lower than 5%, the porosity extracted from image–algorithm analysis should be higher than that of the mercury injection experiment, but the effect of noise reduction makes the porosity positively correlated with the mercury injection experiment parameter. When the porosity of the coal reservoir is high (>5%), the porosity affected by the noise reduction effect is far lower than that of a sample, so that the porosity shows a trend that is originally higher than that of the mercury injection experiment.

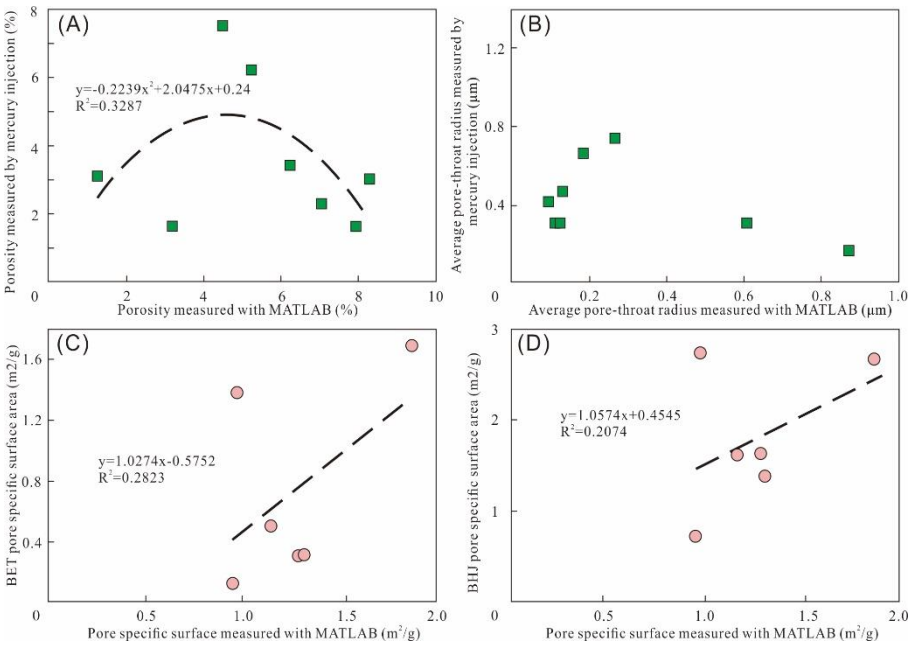

Figure 11. (**A**) The porosity was measured by image–algorithm quantitative analysis with the mercury injection data. (**B**) The average pore-throat radius was measured by image–algorithm quantitative analysis with the mercury injection data. The relationship between specific surface area measured by image–algorithm analysis with BET specific surface area (**C**) and BJH specific surface area (**D**) by N_2 adsorption experiment.

For the pore throat radius, the results based on image analysis are different from those carried out by the mercury injection experiment. Figure 11B shows that when the average

pore radius is less than 200 nm, the pore throat radius measured by the mercury injection experiment is higher than the value calculated based on image–algorithm analysis with a very good linear relationship. However, when the average pore radius is greater than 200 nm, there is no obvious rule. We speculate that the reason for this distribution is mainly due to the difference between the two experimental principles. The measurement target of the mercury injection experiment is the connected pore throat radius of the coal sample, which cannot be measured for some closed and disconnected pores. The image–algorithm analysis method calculates all the pores in the image, including the connected pore space and the closed pores with a smaller radius. The principle of the two methods leads to the larger radius of the pore-throat measured by the mercury injection experiment than that obtained by the image–algorithm analysis.

The specific surface area parameters obtained by the low-temperature N_2 adsorption experiment include BET specific surface area and BJH specific surface area. We establish scatter plots of the specific surface area measured by image–algorithm analysis with BET specific surface area and BJH specific surface area (Figure 10C,D). Figure 10C shows a good positive correlation between the BET specific surface and the specific surface area with R^2 = 0.2823 and a linear coefficient of 1.0274. Similarly, there is a positive correlation between BJH specific surface area and specific surface area with R^2 = 0.2074 and a = 1.0574. As we have discussed, the noise reduction process of image analysis will lead to the disappearance of some small holes, while the BET specific surface and BJH specific surface area measured by the gas adsorption theory model cannot obtain some closed pores. These two experimental conditions just form a complementary condition, which makes the results more similar.

4. Conclusions

Image–algorithm quantitative analysis combines the visualization of SEM imaging and digital image technology to achieve quantitative analysis of pore structure parameters of coal reservoirs. The SEM-based characterization analysis can obtain some pore structure parameters including 2D porosity, pore coordination number, and pore throat ratio, whereas the conventional methods such as N_2 adsorption and mercury injection have obvious advantages in calculating pore radius and porosity in whole rock scale of coal.

Image-algorithm analysis relies on the calculation system for recognition in a convenient and accurate way for 2D images such as SEM and microscopy images. The preliminary sample preparation is the most important for organic-rich samples, especially the sample polishing process. It is suggested that the characterization processing is suitable for coal or other organic-rich porous materials with porosity > 2% and pore radius > 15 nm.

An alternative way to characterize the full-scale pore structure of coal in 2D and 3D requires comprehensive use of multiple methods. Taking our sample as an example, the whole process of quantitative analysis has good identification for analysis when the pore throat radius is higher than 15 nm in most pore types of coal in 2D. Three-dimensional nano-CT and indirect methods such as NMR and high-pressure mercury injection are expected for determination when pore throat radius is lower than 15 nm.

Author Contributions: Conceptualization, M.J.; Methodology, W.H. and Y.L.; Software, W.H.; Writing—original draft, M.J.; Writing—review & editing, W.H.; Project administration, Y.L. All authors have read and agreed to the published version of the manuscript.

Funding: This work was financially supported by the 'National Natural Science Foundation of China (Grant No. 41972172 and No. U1910205).

Data Availability Statement: The data presented in this study are available on request from the corresponding author.

Conflicts of Interest: The authors declare no conflict of interest.

References

1. Karacan, C.O.; Okandan, E. Adsorption and gas transport in coal microstructure: Investigation and evaluation by quantitative X-ray CT imaging. *Fuel* **2001**, *80*, 209–520. [CrossRef]
2. Longinos, S.N.; Wang, L.; Hazlett, R. Advances in Cryogenic Fracturing of Coalbed Methane Reservoirs with LN_2. *Energies* **2022**, *15*, 9464. [CrossRef]
3. Olajossy, A.; Cieślik, J. Why Coal Bed Methane (CBM) Production in Some Basins is Difficult. *Energies* **2019**, *12*, 2918. [CrossRef]
4. Hou, H.; Shao, L.; Tang, Y.; Zhao, S.; Yuan, Y.; Li, Y.; Mu, G.; Zhou, Y.; Liang, G.; Zhang, J. Quantitative characterization of low-rank coal reservoirs in the southern Junggar Basin, NW China: Implications for pore structure evolution around the first coalification jump. *Mar. Pet. Geol.* **2020**, *113*, 104165. [CrossRef]
5. Shan, L.; Liu, C.; Liu, Y.; Kong, W.; Hei, X. Rock CT Image Super-Resolution Using Residual Dual-Channel Attention Generative Adversarial Network. *Energies* **2022**, *15*, 5115. [CrossRef]
6. Zhang, L.; Wei, C.; Nie, Y.; Wang, R. Pressure Measurement of Coal Seam with Active Nitrogen Injection: Model and Experimental Analysis. *ACS Omega* **2022**, *7*, 46935–46945. [CrossRef] [PubMed]
7. Klaver, J.; Desbois, G.; Littke, R.; Urai, J.L. BIB-SEM pore characterization of mature and post mature Posidonia Shale samples from the Hils area, Germany. *Int. J. Coal Geol.* **2016**, *158*, 78–89. [CrossRef]
8. Chen, Y.; Tang, H.; Zheng, M.; Li, C.; Zhao, S.; Zhao, N.; Leng, Y. Fractal Characteristics and Significance of Different Pore Types of the Wufeng–Longmaxi Formation, Southern Sichuan Basin, China, Based on N2 Adsorption and Image Analysis. *ACS Omega* **2021**, *6*, 30889–30900. [CrossRef]
9. Li, Y.; Yang, J.; Pan, Z.; Tong, W. Nanoscale pore structure and mechanical property analysis of coal: An insight combining AFM and SEM images. *Fuel* **2020**, *260*, 116352. [CrossRef]
10. Zhang, L.; Wang, G.; Xue, Q.; Zuo, H.; She, X.; Wang, J. Effect of preheating on coking coal and metallurgical coke properties: A review. *Fuel Process. Technol.* **2021**, *221*, 106942. [CrossRef]
11. Bednarz, M.; McIlroy, D. Organism–sediment interactions in shale-hydrocarbon reservoir facies—Three-dimensional reconstruction of complex ichnofabric geometries and pore-networks. *Int. J. Coal Geol.* **2015**, *150–151*, 238–251. [CrossRef]
12. Pandey, R.; Harpalani, S. An imaging and fractal approach towards understanding reservoir scale changes in coal due to bioconversion. *Fuel* **2018**, *230*, 282–297. [CrossRef]
13. Li, Y.; Cui, H.; Zhang, P.; Wang, D.; Wei, J. Three-dimensional visualization and quantitative characterization of coal fracture dynamic evolution under uniaxial and triaxial compression based on CT scanning. *Fuel* **2020**, *262*, 116568. [CrossRef]
14. Luo, L.; Liu, J.; Zhang, Y.; Zhang, H.; Ma, J.; You, Y.; Jiang, X. Application of small angle X-ray scattering in evaluation of pore structure of superfine pulverized coal/char. *Fuel* **2016**, *185*, 190–198. [CrossRef]
15. Fang, H.; Sang, S.; Liu, S.; Du, Y. Methodology of three-dimensional visualization and quantitative characterization of nanopores in coal by using FIB-SEM and its application with anthracite in Qinshui basin. *J. Pet. Sci. Eng.* **2019**, *182*, 106285. [CrossRef]
16. Jing, Y.; Armstrong, R.T.; Ramandi, H.L.; Mostaghimi, P. Coal cleat reconstruction using micro-computed tomography imaging. *Fuel* **2016**, *181*, 286–299. [CrossRef]
17. Roslin, A.; Pokrajac, D.; Zhou, Y. Cleat structure analysis and permeability simulation of coal samples based on micro-computed tomography (micro-CT) and scan electron microscopy (SEM) technology. *Fuel* **2019**, *254*, 115579. [CrossRef]
18. Wang, G.; Shen, J.; Liu, S.; Jiang, C.; Qin, X. Three-dimensional modeling and analysis of macro-pore structure of coal using combined X-ray CT imaging and fractal theory. *Int. J. Rock Mech. Min. Sci.* **2019**, *123*, 104082. [CrossRef]
19. Steel, K.M.; Dawson, R.E.; Jenkins, D.R.; Pearce, R.; Mahoney, M.R. Use of rheometry and micro-CT analysis to understand pore structure development in coke. *Fuel Process. Technol.* **2017**, *155*, 106–113. [CrossRef]
20. Wang, G.; Qin, X.; Shen, J.; Zhang, Z.; Han, D.; Jiang, C. Quantitative analysis of microscopic structure and gas seepage characteristics of low-rank coal based on CT three-dimensional reconstruction of CT images and fractal theory. *Fuel* **2019**, *256*, 115900. [CrossRef]
21. Hong, Y.-D.; Lin, B.-Q.; Zhu, C.-J.; Wang, Z.; Liu, J.-Q.; Saffari, P.; Nie, W. Image and ultrasonic analysis-based investigation of coal core fracturing by microwave energy. *Int. J. Rock Mech. Min. Sci.* **2020**, *127*, 104232. [CrossRef]
22. Perkins, J.; Williams, O.; Wu, T.; Lester, E. Automated image analysis techniques to characterise pulverised coal particles and predict combustion char morphology. *Fuel* **2020**, *259*, 116022. [CrossRef]
23. Cai, Y.; Li, Q.; Liu, D.; Zhou, Y.; Lv, D. Insights into matrix compressibility of coals by mercury intrusion porosimetry and N2 adsorption. *Int. J. Coal Geol.* **2018**, *200*, 199–212. [CrossRef]
24. Zhang, N.; Wang, S.; Zhao, F.; Sun, X.; He, M. Characterization of the Pore Structure and Fluid Movability of Coal-Measure Sedimentary Rocks by Nuclear Magnetic Resonance (NMR). *ACS Omega* **2021**, *6*, 22831–22839. [CrossRef] [PubMed]
25. Xi, Z.; Tang, S.; Wang, J.; Yang, G.; Li, L. Formation and development of pore structure in marine-continental transitional shale from northern China across a maturation gradient: Insights from gas adsorption and mercury intrusion. *Int. J. Coal Geol.* **2018**, *200*, 87–102. [CrossRef]
26. Gao, F.; Song, Y.; Li, Z.; Xiong, F.; Chen, L.; Zhang, X.; Chen, Z.; Moortgat, J. Quantitative characterization of pore connectivity using NMR and MIP: A case study of the Wangyinpu and Guanyintang shales in the Xiuwu basin, Southern China. *Int. J. Coal Geol.* **2018**, *197*, 53–65. [CrossRef]
27. Bahadori, M.; Bakhshandeh Amnieh, H.; Khajezadeh, A. A new geometrical-statistical algorithm for predicting two-dimensional distribution of rock fragments caused by blasting. *Int. J. Rock Mech. Min. Sci.* **2016**, *86*, 55–64. [CrossRef]

28. Yang, J.; Su, Y.; He, X.; Tan, H.; Jiang, Y.; Zeng, L.; Strnadel, B. Pore structure evaluation of cementing composites blended with coal by-products: Calcined coal gangue and coal fly ash. *Fuel Process. Technol.* **2018**, *181*, 75–90. [CrossRef]
29. Stsepuro, N.; Kovalev, M.; Krasin, G.; Podlesnykh, I.; Gulina, Y.; Kudryashov, S. Surface Depth-Mapping of Material via the Transport-of-Intensity Equation. *Photonics* **2022**, *9*, 815. [CrossRef]
30. Tafesse, S.; Fernlund, J.M.R.; Bergholm, F. Digital sieving-Matlab based 3-D image analysis. *Eng. Geol.* **2012**, *137–138*, 74–84. [CrossRef]
31. Michalak, H.; Okarma, K. Improvement of Image Binarization Methods Using Image Preprocessing with Local Entropy Filtering for Alphanumerical Character Recognition Purposes. *Entropy* **2019**, *21*, 562. [CrossRef] [PubMed]
32. Sarkar, G.; Siddiqua, S. Effect of fluid chemistry on the microstructure of light backfill: An X-ray CT investigation. *Eng. Geol.* **2016**, *202*, 153–162. [CrossRef]
33. Naveen, P.; Asif, M.; Ojha, K. Integrated fractal description of nanopore structure and its effect on CH4 adsorption on Jharia coals, India. *Fuel* **2018**, *232*, 190–204. [CrossRef]
34. Druckrey, A.M.; Alshibli, K.A.; Al-Raoush, R.I. 3D characterization of sand particle-to-particle contact and morphology. *Comput. Geotech.* **2016**, *74*, 26–35. [CrossRef]
35. Xin, F.; Xu, H.; Tang, D.; Cao, L. An improved method to determine accurate porosity of low-rank coals by nuclear magnetic resonance. *Fuel Process. Technol.* **2020**, *205*, 106435. [CrossRef]
36. Fusi, N.; Martinez-Martinez, J. Mercury porosimetry as a tool for improving quality of micro-CT images in low porosity carbonate rocks. *Eng. Geol.* **2013**, *166*, 272–282. [CrossRef]
37. Yoshizawa, N.; Yamada, Y.; Furuta, T.; Shiraishi, M. Coal-Based Activated Carbons Prepared with Organometallics and Their Mesoporous Structure. *Energy Fuels* **1997**, *11*, 327–330. [CrossRef]
38. Zhou, S.; Liu, D.; Cai, Y.; Yao, Y.; Li, Z. 3D characterization and quantitative evaluation of pore-fracture networks of two Chinese coals using FIB-SEM tomography. *Int. J. Coal Geol.* **2017**, *174*, 41–54. [CrossRef]
39. Lu, Y.; Chen, X.; Tang, J.; Li, H.; Zhou, L.; Han, S.; Ge, Z.; Xia, B.; Shen, H.; Zhang, J. Relationship between pore structure and mechanical properties of shale on supercritical carbon dioxide saturation. *Energy* **2019**, *172*, 270–285. [CrossRef]
40. Zhu, H.; Ju, Y.; Huang, C.; Chen, F.; Chen, B.; Yu, K. Microcosmic gas adsorption mechanism on clay-organic nanocomposites in a marine shale. *Energy* **2020**, *197*, 117256. [CrossRef]